Seismic migration processing of *P-SV* converted phases for mantle discontinuity structure beneath the Snake River Plain, western United States

Anne F. Sheehan

Department of Geological Sciences, University of Colorado, Boulder

Peter M. Shearer

Scripps Institution of Oceanography, La Jolla, California

Hersh J. Gilbert and Kenneth G. Dueker

Department of Geological Sciences, University of Colorado, Boulder

Abstract. We experiment with backprojection migration processing of teleseismic receiver functions from the Snake River Plain (SRP) broadband seismic experiment. Previous analyses of data from this experiment have used a common midpoint (CMP) stacking approach, a method widely applied for analysis of *P-SV* converted phases (receiver functions) to obtain high-resolution imaging of upper mantle discontinuities. The CMP technique assumes that all *P-SV* conversions are produced by flat-lying structures and may not properly image dipping, curved, or laterally discontinuous interfaces. In this paper we adopt a backprojection migration scheme to solve for an array of point scatterers that best produces the large suite of observed receiver functions. We first perform synthetic experiments that illustrate the potential improvement of migration processing over CMP stacks. Application of the migration processing to the SRP data set shows most of the major features as in the original CMP work, but with a weaker 410-km discontinuity and a more intermittent discontinuity at 250 km apparent depth. Random resampling tests are also performed to assess the robustness of subtle features in our discontinuity images. These tests show that a 20-km elevation of the 660-km discontinuity directly beneath the Snake River Plain is robust, but that the variations in 410-km discontinuity topography that we observe are not stable upon resampling. "Bright spots" near 250 km apparent depth are robust upon resampling, but interpretation of these features is complicated by possible sidelobe artifacts from topside Moho reverberations.

1. Introduction

Common midpoint (CMP) stacking of records of *P-SV* converted phases (receiver functions) has become a popular technique for detailed imaging of mantle discontinuities [e.g., *Dueker and Sheehan*, 1997, 1998; *Li et al.*, 1998a; *Shen et al.*, 1998b; *Gurrola et al.*, 1998]. By stacking many receiver functions that sample nearly the same subsurface point, signal to noise is dramatically improved and small-amplitude features can be resolved. These techniques have led to high-resolution images of mantle discontinuity topography, demonstrating that the topography can be significant (20 to 30 km) over wavelengths of a few hundred kilometers. The CMP technique assumes that the *P-SV* conversions are produced by horizontal, laterally continuous structures and does not take into account diffraction effects and focusing produced by dipping or laterally discontinuous interfaces. Work from the German Continental Drilling Program (KTB) deep drill hole has further shown how CMP seismic reflection stacking enhances horizontal reflectivity

and can produce misleading crustal images [*Harjes et al.*, 1997]. The seismic reflection community has long recognized the importance of migrating reflected phases back to their appropriate origin point. Seismic migration eliminates artifacts produced by inappropriate assumptions of horizontal planar structure and typically produces significant improvements in reflection image quality [e.g., *Claerbout*, 1992]. Recently migration techniques have been extended to receiver function images [e.g., *Ryberg et al.*, 1998; *Bostock and Rondenay*, 1999], SS precursors [*Shearer et al.*, 1999] and to other seismic data sets [e.g., *Revenaugh*, 1995].

Here we experiment with migration techniques applied to receiver functions, with particular application to data from the Snake River Plain (SRP) Program for the Array Seismic Studies of the Continental Lithosphere (PASSCAL) seismic experiment [*Dueker and Humphreys*, 1993]. Synthetic experiments presented here show that improvement over simple CMP stacking can be achieved through backprojection migration processing applied to receiver functions.

2. Data and Prior Work

The Snake River Plain (SRP) PASSCAL seismic experiment consisted of the deployment of 25 three-component broadband
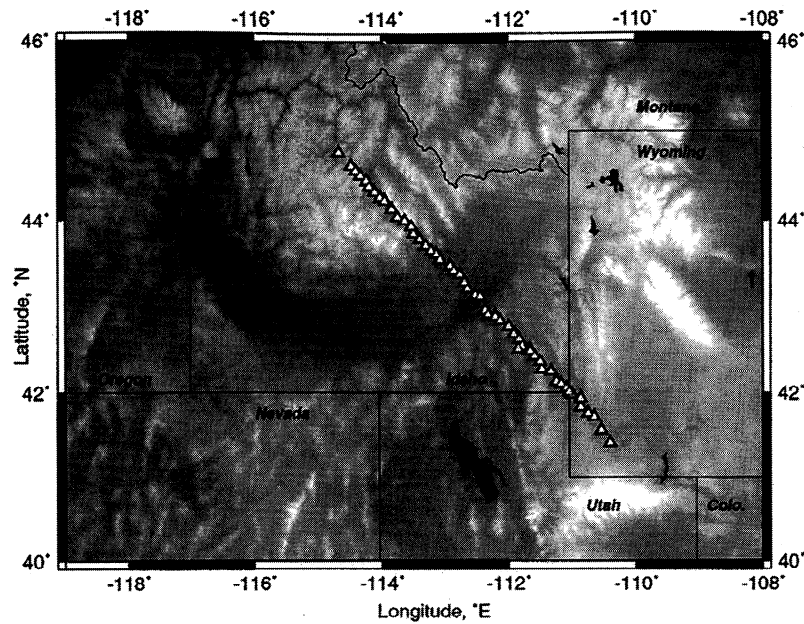
Figure 1. Seismograph stations of the Snake River Plain PASSCAL experiment on shaded map of topographic relief. Triangles indicate station locations.

and short period seismometers for a 6-month period in 1993 (Figure 1). The seismometers were sited in a northwest–southeast oriented line just over 500 km long. An average station spacing of 10 km was achieved by moving the stations during the experiment, giving a total of 54 sites occupied. The geometry of the line array was designed to align with the dominant arrival azimuths for earthquakes to the northwest (Alaska, Kuriles, west

Pacific) and southeast (South and Central America) Here, we analyze seismograms from along-line earthquakes with epicentral distances from 27° to 95° (see Figure 2 for earthquake locations). We compute receiver functions for seismograms with clear *P* wave arrivals on both vertical and radial components through frequency domain deconvolution of the vertical component from the radial. Before deconvolution the seismograms are windowed
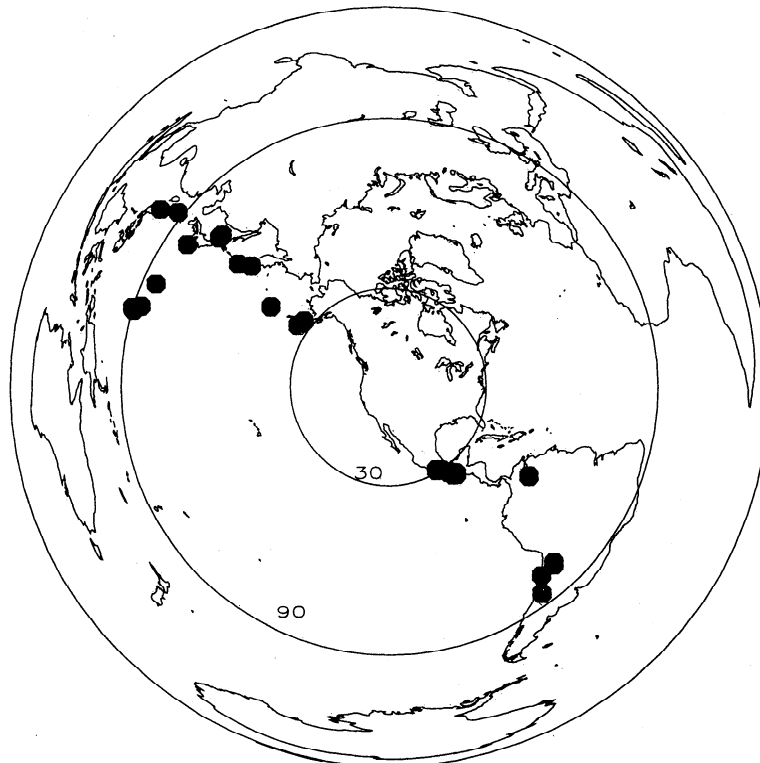

Figure 2. Distribution of earthquakes used in receiver function study. Circles of radius 30° and 90° are shown, centered on the Snake River Plain. Lambert projection.

from 5 s before to 100 s after the first break of the *P* wave arrival using a cosine tapered boxcar window. Seismograms from events at distances less than 38° with visible *PP* arrivals are not used. Receiver functions are calculated as by *Dueker and Sheehan* [1997]. The deconvolution is accomplished by spectral division using a water level setting of 0.1. After division, the components of ground motion are inverse Fourier transformed. The receiver functions are further filtered from 10 to 40 s for this study. Only receiver functions with a clear radial *P* arrival are retained. The amplitude of the direct *P* wave on the resulting receiver function is normalized to one. Frequency analysis, where receiver function images are calculated for various filter bands was performed by *Dueker and Sheehan* [1997] and is not repeated here.

A random subset of 16 receiver functions from our total data set of 420 receiver functions is shown in Figure 3 and illustrates how the 410- and 660-km discontinuity converted phases, expected at ~50 s and 70 s, are not clearly visible in the raw receiver functions. *Dueker and Sheehan* [1997] achieved an improved signal-to-noise ratio by performing common depth point (CMP) stacking of the receiver functions (more accurately referred to as common conversion point or CCP stacking, but usually called CMP stacking because of the easily recognized industry analogue). With CMP stacking, it is hoped that noise is largely incoherent among individual receiver functions so that it will be reduced in multitrace stacks, while coherent signals, such as *Pds* conversions, will stack constructively. Sources of noise on single traces include topographic scattering and complex *P-S* resonance in sedimentary basins. The CMP stacking procedure consists of grouping receiver functions geographically by the subsurface regions that the rays sample, applying normal moveout corrections to account for timing variations due to different source-receiver separations, correcting for crust and upper mantle lateral heterogeneity by applying appropriate time shifts to individual seismograms (analogous to the statics correction in reflection seismology) and stacking. Further details on the CMP stacking procedure are given by *Dueker and Sheehan* [1997]. Results of the CMP stack of the SRP data reveal 20-30 km of topography on the 410- and 660-km discontinuities over 200-300 km lateral scale lengths, as well as a strong apparent *Pds* conversion near 250 km depth.

The receiver function observations have differing signal-to-noise ratios, and a choice must be made between selecting a small number of clean, low-noise records and larger numbers of records of more variable quality. Our data selection criteria required a strong *P* arrival on the radial receiver function, a coda standard deviation <0.45 of the *P* amplitude, and a source back azimuth within 20° of the station line (usually 10° in practice). The records retained also passed two levels of visual inspection, both before and after deconvolution. This resulted in 420 receiver functions from the Snake River Plain data set. In contrast, *Beucler et al.* [1999] recently analyzed 260 receiver functions from the SRP experiment, applying a stricter criterion that
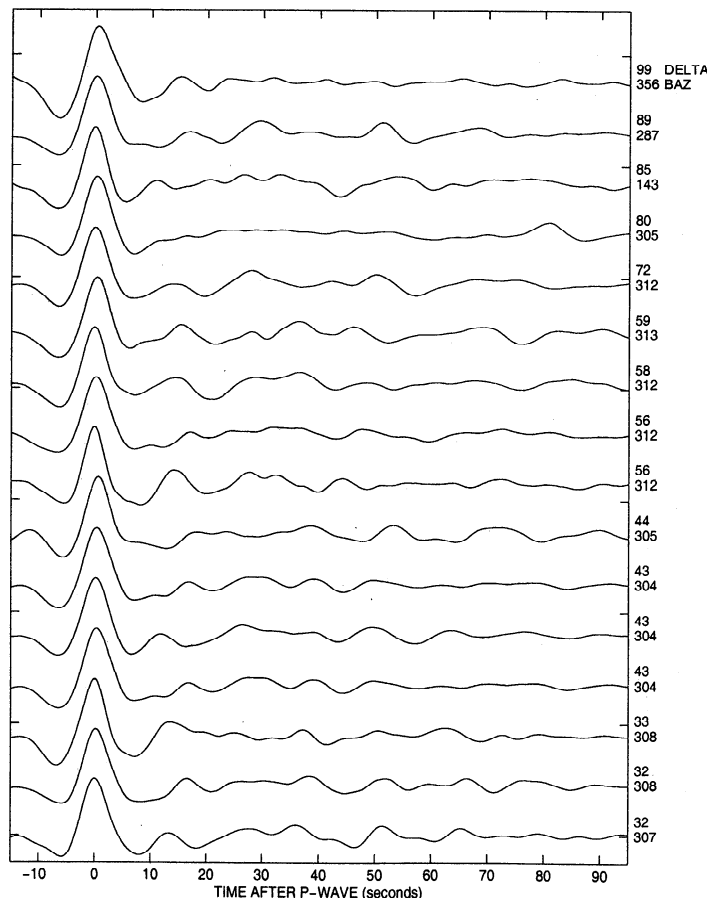
Figure 3. A sampling of 16 of the 420 low-pass-filtered individual radial receiver functions used in this study. The epicentral distance and back azimuth from the recording station to the earthquake are given to the right of each trace. Few arrivals besides direct *P* at time 0 are visible on the individual receiver functions.

required a coda amplitude <15% of the radial receiver function amplitude. For our backprojection technique it is desirable to have as many different ray paths as possible, even if the record quality is less than ideal. As seen in Figure 3, the individual receiver functions are highly variable, but after processing many records (Figure 6 and others), coherent patterns emerge. The stability of our results is best evaluated using random resampling tests (see section 4.2); these tests show that errant receiver functions are not controlling our solutions.

## 3. Receiver Function Migration

The CMP stacking approach implicitly assumes that the *P*-to-*SV* conversions occur along a horizontal interface so that the discontinuity conversion points are consistent with ray paths that obey Snell's law. Thus dipping or intermittent discontinuities may not be correctly imaged. To obtain improved results, migration techniques can be applied that account for the possibility of diffraction or scattering from nonhorizontal and laterally discontinuous structures. These methods have long been used in reflection seismology. Here we develop a simple form of migration suited to the receiver function imaging problem.

3.1. Forward Problem

We characterize the model as a grid of isotropic point scatterers of known position and amplitude (Figure 4) over function at the *j*th station from the *i*th event, S_{ij}, is modeled as the sum of *P*-to-*S* conversions at any of these *k* points, or

$$S_{ij}(t) = f_i(t) * \sum_{k=1,m} \frac{\delta(t - t_{ik}^P - t_{kj}^S)\phi_{ijk}}{r_{ik}r_{kj}} M_k, \qquad (1)$$

where $f_i(t)$ is the effective source-time function function (i.e., the response that a delta function input would produce following filtering and receiver function deconvolution), t_{ik}^P is the source-to-scatterer *P* wave travel time, t_{kj}^S is the scatterer-to-receiver *S* wave travel time, ϕ_{ijk} describes the angular dependence of the

station *j*

model point *k*

from event *i*
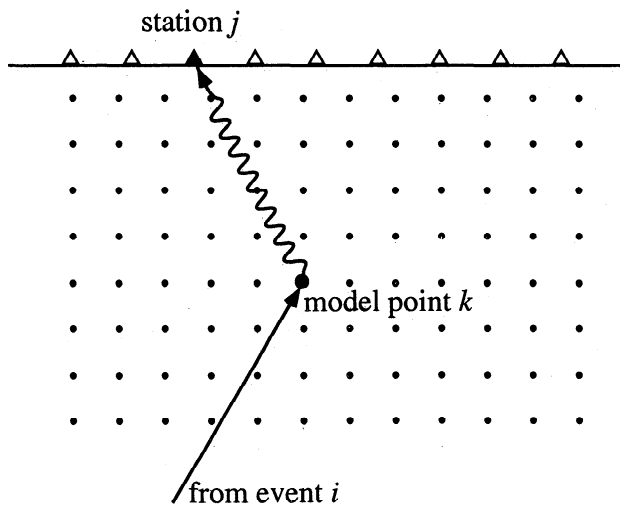
Figure 4. Schematic illustration of geometry used in migration inversion. A grid of point scatterers is defined, and timing information for each source-scatterer-receiver combination is tabulated, with source-scatterer as a *P*-leg and scatterer-receiver as an *S*-converted wave. Scatterer strength is estimated by summing data along the *P*-to-*S* scattered-wave travel time curve with corrections for geometrical spreading.

scattering (here we assume $\phi_{ijk} = 1$), $1/r_{ik}$ and $1/r_{kj}$ are the source-to-scatterer and scatterer-to-receiver geometrical spreading factors, and M_k is the scattering strength at model point *k*. We assume that the model points are uniformly spaced; otherwise, a term for the effective volume of each model point would also be required. From Kirchhoff theory, $f'(t)$ is the derivative of the source-time function for a three-dimensional model but is given by the "half derivative" in the case of the two-dimensional model used here [e.g., *Kampfmann*, 1988]. All times given are relative to the direct *P* time, and amplitude of the direct *P* arrival on the radial receiver functions is normalized to one.

3.2. Simplifications

We compute the travel times using ray theory applied to the IASP91 model [*Kennett*, 1991]. We assume the effective source-time function $f(t)$ is constant for all receiver functions and use an empirical $f(t)$ obtained from a stack of the data. We assume that r_{ik} is constant over *k* since the model is relatively small compared to the distance to the sources. We approximate r_{kj} as the scatterer-to-receiver distance. By stringing the individual receiver functions end-to-end into a data vector **d**, equation (1) may be written in matrix form as

$$\mathbf{d} = \mathbf{Gm}, \qquad (2)$$

where **m** is a model vector containing the scattering amplitudes and **G** is a matrix that contains the timing and geometrical spreading factors (i.e., the right-hand-side of (1), excluding the M_k term). Typically, **G** will be a large, sparse matrix that can be efficiently stored on the computer by only saving its nonzero elements. Inclusion of the source-time function directly in **G** greatly increases the number of non-zero elements. To avoid this, we leave $f(t)$ out of **G** and perform the convolutions separately as required.

We consider only relative amplitudes in the model; that is, we do not attempt to relate the observed seismic amplitudes to specific velocity and density changes in the model. We also assume that the model structures are two-dimensional and constant in the direction perpendicular to orientation of the receiver array.

3.3. Inversion for Model

An approximate solution to (2) is given by

$$\mathbf{m} = \mathbf{G}^T \mathbf{d}. \qquad (3)$$

This is effectively the backprojection of each point in the receiver functions to the model points that could have produced a scattered arrival at the correct time. Thus each model parameter is simply a weighted sum of the data points (receiver function amplitudes) which could have scattered from that model point. This approach is very similar to Kirchoff migration methods commonly applied in reflection seismology.

4. Results

4.1. Synthetic Experiments

In order to test the migration processing procedure, we performed a number of synthetic experiments. We assumed a model containing a regional 220-km discontinuity, a flat 410-km
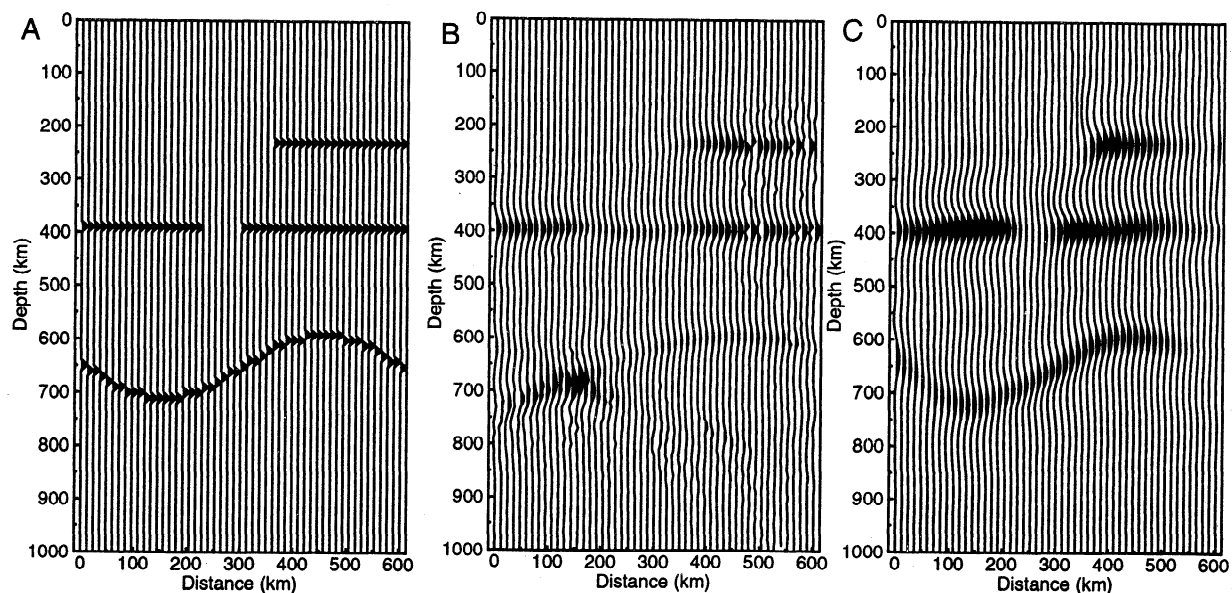
discontinuity with a small gap, and an undulating 660-km discontinuity (Figure 5a). Using (2), we generated synthetic seismograms using the same source and receiver geometries as in the SRP experiment and then computed common midpoint stacks of the synthetic receiver functions (Figure 5a). The CMP stacking was performed by projecting the points on the seismograms back to their ray theoretical *P-to-SV* conversion points (assuming horizontal interfaces and Snell's law) and averaging the results within 50-km-wide bins. Focusing and diffraction artifacts are obvious in the synthetic CMP image. The 410-km discontinuity appears as a continuous feature, and the small gap is not recovered. The undulating 660-km discontinuity displays a classic "bow-tie" or "frown" diffraction pattern, and the sharp edge of the 220-km discontinuity appears as a half bow-tie. In contrast, the backprojection migration of the synthetic receiver functions (shown in Figure 5c) recovers the starting model much more clearly, including the gap in the 410-km discontinuity and the large undulation on the 660-km discontinuity. The amplitudes of the features at the right-hand (southeast) side of the image are faint owing to poor ray coverage in this area caused by a lack of high-quality records of events to the southeast at stations on the southeast end of the array (see Figure 2 of *Dueker and Sheehan* [1997] for plot of ray coverage).

This synthetic experiment almost certainly exaggerates the resolution that can be achieved with real data because it ignores the effect of noise and assumes that the forward problem is perfectly known (in this respect it is similar to "checkerboard" tests often applied in tomography studies). Nonetheless, it is useful for assessing the limitations imposed by the available ray coverage and highlighting the advantages of backprojection over CMP stacking in the case of nonhorizontal structures. We have also performed synthetic experiments for tighter station distributions (of the order of 1-2 km station spacing) designed for

high-resolution imaging of crustal and upper mantle discontinuity [*Sheehan et al.*, 1999] with good results. We find that the migration results are not as sensitive to station geometry as are the CMP results, and similar results are achieved with a variety of array designs. A one-to-one lateral array extent to target depth works well in the synthetic experiments, despite the rules of thumb for reflection migration that suggest that a much larger lateral extent relative to target depth is needed.

### 4.2. Application to Snake River Plain Data

The migration processing is next applied to the receiver function data from the Snake River Plain experiment. We use the same raw receiver functions as computed in the CMP stacking analysis of *Dueker and Sheehan* [1997] and apply lateral heterogeneity corrections as timing shifts to the traces, following the procedure outlined by *Dueker and Sheehan* [1997]. Unlike the approach used in the CMP stacks, each receiver function is treated individually in the backprojection migration, and no stacking or explicit normal moveout correction is required. The model consists of a 800-km lateral by 1000-km vertical grid of point scatterers, with spacing between scatterers of 10 km. For each model point, the time of a *Pds* conversion originating at the scatterer for each earthquake-station pair is determined. This timing information makes up the data kernel matrix $\mathbf{G}$ as described in (1) and (2). The two-dimensional grid of scatterers makes up the model vector $\mathbf{m}$, and the data vector is constructed from all of the radial receiver function time series placed end to end. Values $S_{ij}(t)$ of the data vector correspond to samples of the seismogram from source-receiver pair ij at time t ($t = 1, 2, ..., n_{ij}$). Element $G_{(ij)k}$ of the data kernel corresponds to the time on the ijth seismogram (S_{ij}) that model scatterer m_k would contribute to. In our case, 420 seismograms (receiver functions) of length

Figure 5. Synthetic experiments with migration seismic processing of receiver functions. (a) Model containing regional 220-km discontinuity, a flat 410-km discontinuity with a small gap, and an undulating 660-km discontinuity. Synthetic seismograms are generated using the same source and receiver geometries as in the Snake River Plain PASSCAL experiment. (b) Common midpoint stack of synthetic receiver functions. Focusing and diffraction artifacts are obvious. (c) Backprojection migration of synthetic receiver functions. The starting model is recovered well, including the gap in the 410-km discontinuity and the large undulation on the 660-km discontinuity. Note that there is no vertical exageration in this or any of the subsequent cross sections.

1200 points (240 s) make up a 504,000 element data vector, and the grid of 8000 model scatterers makes up the model vector **m**.

Results of the backprojection migration are shown in Figure 6, along with the original CMP image. The original CMP stacking (Figure 6a) was performed by ray tracing the converted *S* wave ray paths to 400- and 700-km binning depths. After tracing the converted *S* wave ray set downward, the converted *S* wave ray "piercing points" at a chosen depth (e.g., 400 and 700 km depth) are geographically binned. The bins are 75 km wide and spaced every 25 km, resulting in a 50% overlap between bins. Receiver functions which sample a given bin are then are then stacked along normal move-out curves for the tectonic North America
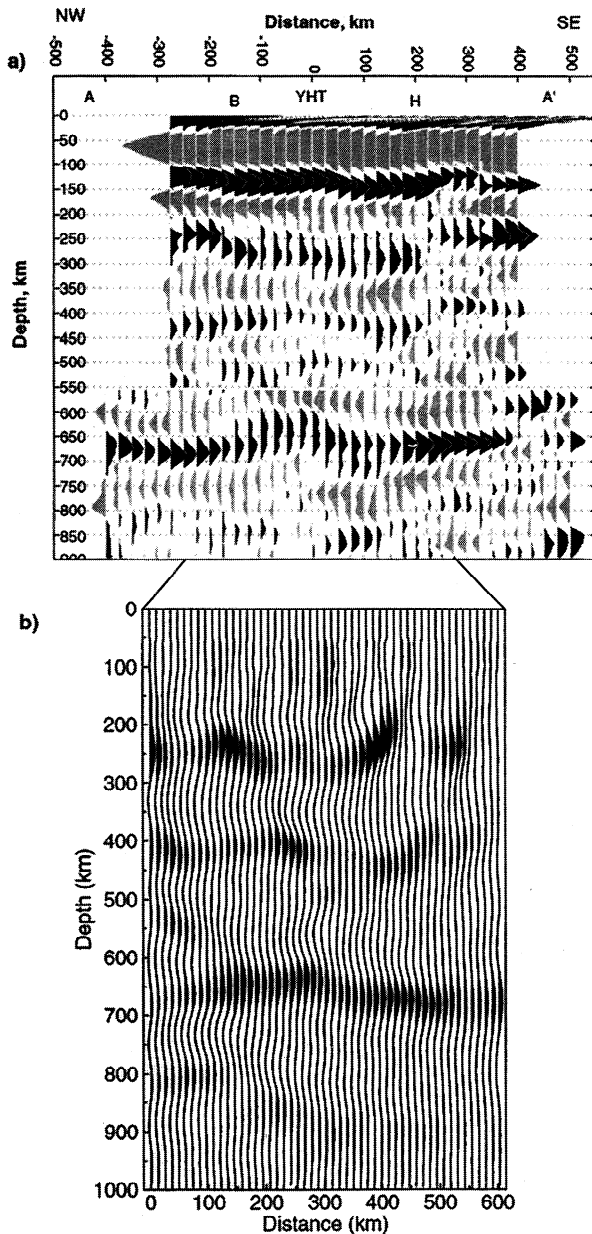

Figure 6. (a) Discontinuity image from Snake River Plain PASSCAL experiment data [*Dueker and Sheehan*, 1997]. Each trace shown represents a common midpoint stack (CMP) of all receiver functions within a 75-km-wide bin stacked along appropriate normal move-out curves and with lateral heterogeneity corrections applied before the stack. Positive and negative polarity energy are plotted in solid and shaded, respectively. (b) Migrated Snake River Plain discontinuity image.

(TNA) shear velocity model [*Grand and Helmberger*, 1984] after time shifting the individual traces to correct for upper mantle lateral heterogeneity [*Dueker and Sheehan*, 1997]. The main features of both images are similar, such as the strong 660-km discontinuity with ~30 km of topography over 400-500 km wavelength, a weaker 410-km discontinuity, and a strong signal which migrates to ~250 km depth. A weak 520-km discontinuity, which was visible in the CMP image, is not apparent in the migrated image except as a dipping fragment at 0-100 km *x* offset and possibly as a shallow section from 300 to 400 km *x* offset (note that all *x* offsets discussed in text refer to the scale on Figure 6b). The 250-km depth "discontinuity" is sharpened in the migrated image and appears as a series of high-amplitude "bright spots" rather than as a laterally continuous feature. Note that the strong layer seen at ~150 km depth in the CMP image is an artifact arising from the $2p1s$ Moho reverberation [see *Dueker and Sheehan*, 1997]. To avoid projecting this high-amplitude feature into the migrated model, we zero the first 60 s of the receiver functions (includes 40 s before and 20 s after the direct P arrival); this accounts of the absence of the 150-km feature in this image.

The discontinuity topography imaged by *Dueker and Sheehan* [1997] is modest compared to our synthetic model topography (Figure 5) so it is not surprising that the migrated and CMP stacked results are in general agreement. One difference is that the migration seems to resolve amplitude variations or gaps in the discontinuities which are smoothed into continuous features in the CMP stacks. This is particularly striking for the apparent 250-km discontinuity. Another likely CMP artifact that is removed by the migration is the apparent broadening of the 660-km discontinuity at 200–300 km *x* offset. Such broadening is likely a diffraction artifact from discontinuity topography [e.g.,*Van der Lee et al.*, 1994].

Given the low signal-to-noise ratios of individual receiver functions and irregular ray sampling, it is important to assess which imaged structures are robust with respect to variations in the available data. A convenient method for determining model uncertainties is provided by random resampling tests. These tests have recently been performed in a number of different ways in seismic imaging analyses [e.g., *Shearer*, 1993; *Revenaugh*, 1995; *Bostock*, 1996; *Dueker and Sheehan*, 1998; *Shearer et al.*, 1999]. Here we implement a bootstrap approach [e.g., *Efron and Tibshirani*, 1991] in which we randomly select receiver functions from the data to create a new population with the same total number of receiver functions as in the original population (resampling with replacement). Thus some receiver functions are not included, and others are included multiple times. The new random subset of receiver functions is processed and migrated in the exact same manner as the full data set, following equations (1)-(3).

The migration results from six sample random resampled data sets are shown in Figure 7. Many more bootstrap iterates were performed than are shown here. Comparisons among the different images show which features are stable with respect to random variations in the data. Common features are a strong 660-km discontinuity from 100 to 600-km *x* offset, and three "bright spots" at 250 km depth at 100-200, 350-420, and 500-550 km *x* offset. The "upwarp" on the 660-km discontinuity at 200-300 km *x* offset originally imaged by *Dueker and Sheehan* [1997] is consistent upon random resampling, indicating that it is a robust feature. The 410-km discontinuity is weak, and the topography on it changes from relatively flat in Figure 7b to showing 50 km or more of topography in Figure 7e. In particular, the intriguing
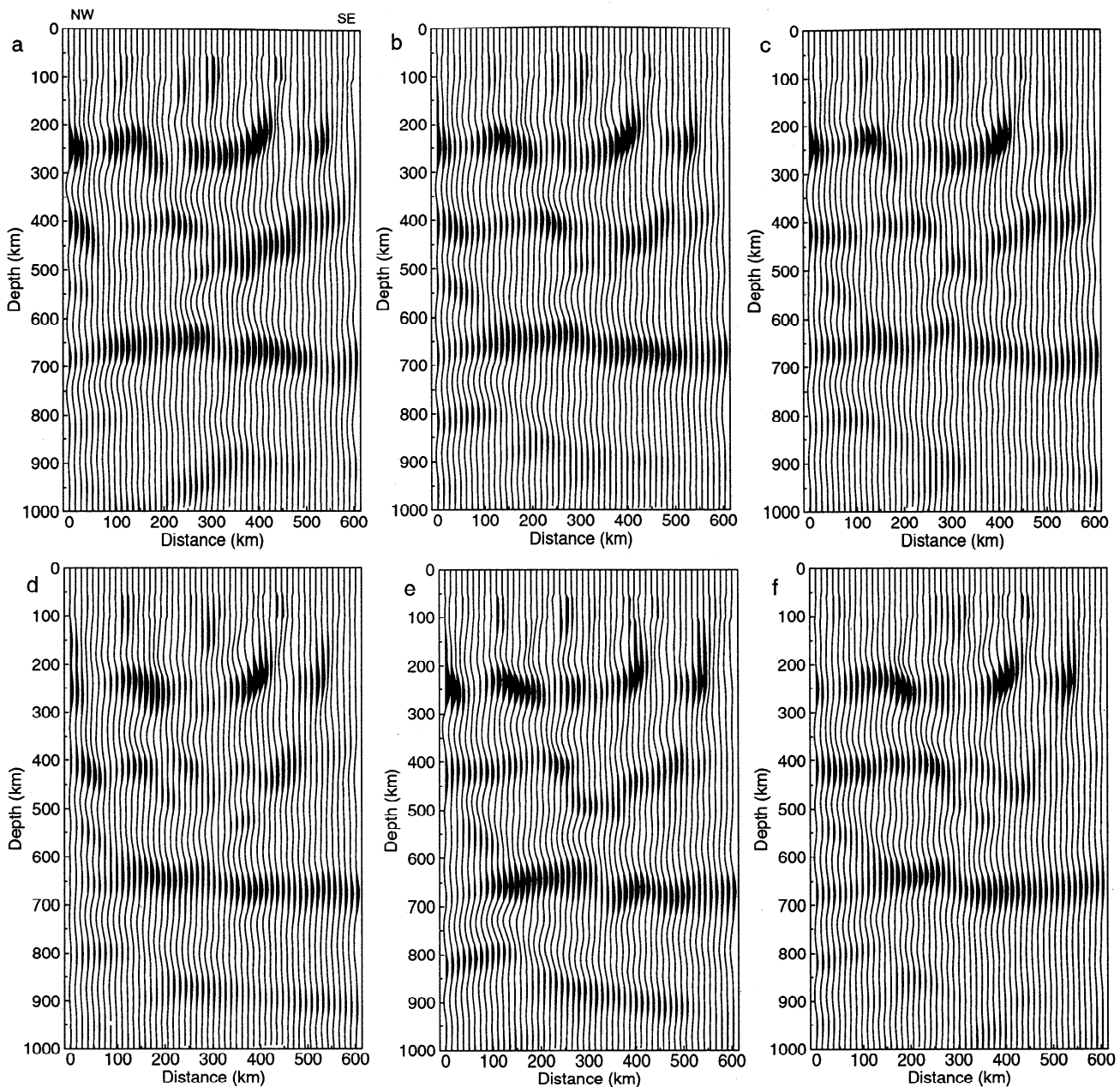
Figure 7. Migration inversion applied to six random subsets of the Snake River Plain receiver functions. Compare to Figure 6b.

depression on the 410-km discontinuity seen in Figures 6a and 6b at 300-400 km x offset is not consistent upon resampling, showing up clearly in only Figure 7c. Clearly, topography such as this that changes upon random resampling is not reliably resolved.

These results demonstrate the importance of random resampling tests for assessing the reliability of seismic images and to avoid overinterpretion of subtle features in the data. Such tests may not be necessary for active-source seismic reflection surveys in which vast numbers of seismograms are processed. However, they are vital for typical passive seismic experiments (e.g., receiver functions, *SS* precursors), in which only hundreds to thousands of records are available, and should be standard in analyses of these data. When results are presented without

reliability tests [e.g., *Kosarev et al.*, 1999], it is difficult to evaluate which features in the images should be trusted.

5. Interpretation

Comparisons of our random resampling plots (Figure 7) with the migrated results from the full data set (Figure 6) help facilitate our interpretations (Figure 8). Because the Clayperon slopes for the mineralogical phase transitions associated with the 410- and 660-km discontinuities are of opposite sign [e.g., *Bina and Helffrich*, 1994], the depths of the 410- and 660-km discontinuities should be anticorrelated in regions where the temperature varations are vertically coherent through the transition zone between the discontinuities. That is, a thinner
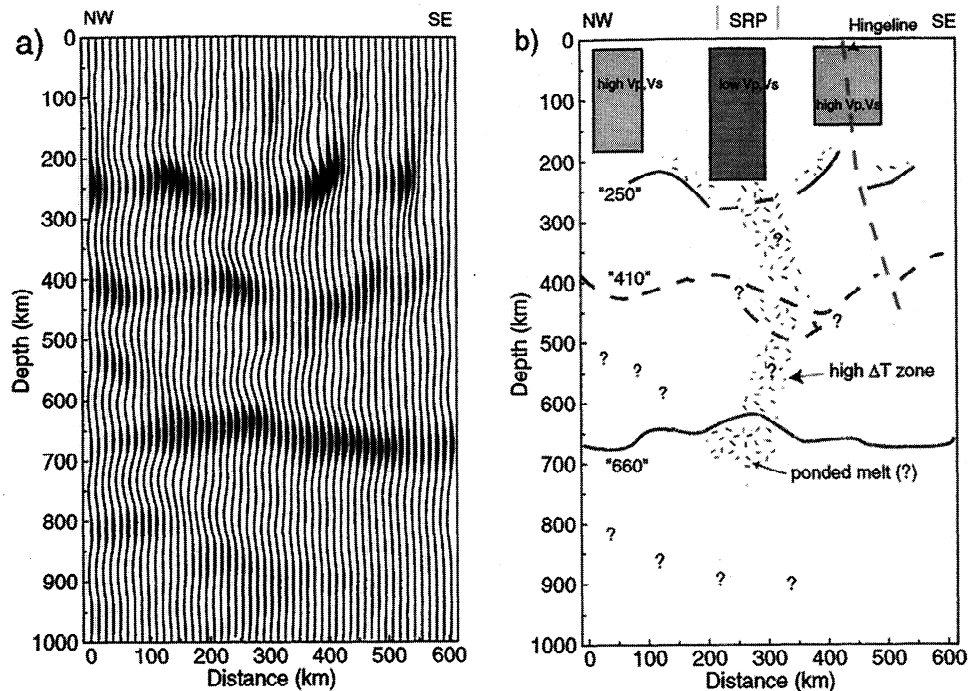
Figure 8. Migrated receiver function image of the Snake River Plain and its interpretation. (a) Migrated receiver function image. (b) Interpretation cartoon. Dark shaded box shows zone of low *P* and *S* wave velocities flanked by zone of high velocities (light shaded boxes) from the tomographic work of *Saltzer and Humphreys* [1997] and *Schutt et al.* [1998]. The velocity contrast is 5% for *P* waves and 8% for *S* waves. The hinge line is shown to offset the 250- and 410-km discontinuities. Zones of suggested higher than normal temperature are given by hashures. Ponded melt in combination with high temperatures is shown elevating the 660-km discontinuity. High temperatures are shown continuing vertically upward to the depressed 410-km discontinuity and eventually connecting with the upper mantle low-velocity region beneath the Snake River Plain (SRP).

mantle transition zone should be observed in regions with warmer than normal mantle, and a thicker mantle transition zone should occur in regions with cool mantle. Topography on these phase boundaries consistent with cool mantle has been observed locally near subduction zones [*Vidale and Benz*, 1992; *Wicks and Richards*, 1993; *Castle and Creager*, 1997; *Collier and Helffrich*, 1997; *Flanagan and Shearer*, 1998b] and a thinner transition zone suggesting warm mantle beneath Iceland [*Shen et al.*, 1998b]. However, recent results from *SS* precursor studies [*Gu et al.*, 1998; *Flanagan and Shearer*, 1998a] suggest that 410- and 660-km discontinuity topography is essentially uncorrelated at global scales (>1000 km wavelength).

We observe ~30 km of topography on the 660-km discontinuity beneath the Snake River Plain array, including a 20-km shallowing at 200-300 km *x* offset. If interpreted solely in terms of temperature, this 20-km upwelling implies a 250°C thermal anomaly, assuming typical Clapeyron slope values from *Bina and Helffrich* [1994] for the γ-spinel to perovskite + magnesiowustite transition expected at the 660-km discontinuity. The shallowing of the 660-km discontinuity is laterally coincident with the slow upper mantle velocities imaged by *Saltzer and Humphreys* [1997] and *Schutt et al.* [1998] beneath the Snake River Plain. This region of elevated 660-km topography is present regardless of upper mantle lateral heterogeneity corrections. In other words, it is a large signal that is not an artifact of an inadequate lateral heterogeneity correction. There is a strong velocity-depth trade-off in receiver function analysis, and some of the discontinuity topography that we observe could be moderated by transition zone velocity variations. However, large lateral velocity heterogeneities over very small scale lengths in the transition zone would be required to produce such apparent topography.

The warmer than normal temperatures implied by the elevated 660-km discontinuity are consistent with, but do not require, the presence of a deep mantle source for the Yellowstone hotspot, or plume material left ponded since the plume was beneath the array since 6-8 Ma. Such a deep mantle source would also be expected to cause a downward deflection of the 410-km discontinuity. The 410-km discontinuity is complex at the *x* offsets coincident with the 660-km discontinuity zone of upwelling, but the nature of this complexity is uncertain, as the features are not consistent upon random resampling. The random resampling tests variously show a gap in the 410-km discontinuity, a depression of 50 km, and a weak 410-km discontinuity in the 300-400 km *x* offset region. Other potential contributors to mantle discontinuity topography include hydration effects [*Wood*, 1995], kinetic effects [*Solomatov and Stevenson*, 1994], and compositional effects [*Anderson*, 1989].

At shallower depth, several "bright spots" at roughly 250 km depth are prominent (Figures 6b and 8). These features are robust upon resampling (Figure 7). The move-out of arrival time with ray parameter from a discontinuity at this depth is not large, and it is difficult to distinguish whether this feature is direct *Pds* from a 250-km-depth discontinuity or a topside reverberation from shallower layers. We have performed phasing analysis [*Dueker and Sheehan*, 1997], which indicates that these arrivals stack to nearly the same amplitude along either direct or reverberation move-out curves. Possible topside reverberations that could

arrive near the time of *P250s* include the *2s1p* Moho reverberation and the *2p1s* reflection if a layer existed at roughly 70 to 90 km depth. The latter possibility seems unlikely as visual inspection of both raw and stacked receiver functions does not show evidence for a spatially coherent direct arrival in the 70-90 km depth range. High-frequency stacks show intermittent arrivals in this depth range only at the edges of the array.

The possibility of contamination from the *2s1p* Moho reverberation, however, cannot so easily be dismissed. Although the polarity of the *2s1p* arrival is negative compared to that of direct *P* (and *2p1s*), positive sidelobes of *2s1p* will arrive near the time of *P250s* (particularly in our 0.03 to 0.1 Hz filtered data) as indicated by synthetic receiver function calculations (M. Bostock, personal communication, 2000). Moho topography and/or crustal focusing effects potentially could produce the observed brightness variations in this feature. Thus it is not clear if our data necessarily require any structure near 250 km; further study, including detailed synthetic seismogram modeling, will be required to address this issue.

Evidence for a discontinuity at ~250 km depth has, however, been noted in many other recent high-resolution receiver functions studies from a wide variety of tectonic environments including mid-ocean ridges [*Shen et al.*, 1998a], ocean islands [*Vinnik et al.*, 1997], subduction zones and back arc settings [*Gilbert et al.*, 1998], continental rift zones [*Gurrola et al.*, 1998], and cratonic shields [*Li et al.*, 1998b]. Some authors have hypothesized that the 250-km discontinuity may represent the base of the asthenospheric low velocity zone [*Lehmann*, 1959, 1961; *Anderson*, 1979]. It has also been suggested that a fabric-based boundary zone between anistropic media above and isotropic material below could produce a discontinuity at this depth [*Revenaugh and Jordan*, 1991; *Gaherty and Jordan*, 1995]. If this is the case, the anisotropy associated with such a model should produce a strong tangential component of motion on the *Pds* phases. We have inspected our tangential component receiver functions and do not see strong or coherent arrivals that would be consistent with this model. However, a more systematic analysis of the tangential component receiver functions is warranted.

If the apparent 250-km reflector imaged in our data represents the base of the low-velocity zone, the topography we observe indicates that the solidus is depressed directly beneath the SRP. Stolper and others [*Stolper et al.*, 1981; *Rigden et al.*, 1984; *Miller et al.*, 1991; *Agee and Walker*, 1988; *Gaetani et al.*, 1998] have suggested that melt becomes anti-buoyant at pressures above 6 to 10 Gpa (~180 to 300 km depth). Their work suggests that under certain circumstances, deep melts may become neutrally to negatively buoyant and concentrate at depth in the Earth. If the 250-km discontinuity acts as a compositional or mechanical barrier to downward migration of the melt, this may help to explain the strong positive shear wave impedance contrast observed from this depth. *Revenaugh and Sipkin* [1994a,b] have described a negative impedance contrast at 330 km depth beneath eastern China, suggesting that it is the top of a melt zone which has accumulated upon the 410-km depth olivine to β phase transition. Beneath the Snake River Plain, the 250-km discontinuity is strong on the flanks of the SRP, where upper mantle velocities are relatively fast [*Saltzer and Humphreys*, 1997], and weaker in amplitude and downwarped directly beneath the SRP, where low upper mantle velocities are imaged. The weak 250-km reflector beneath the central SRP may indicate high temperatures or melt both above and below the

discontinuity, reducing the impedance contrast across it. However, these hypotheses must remain speculative until more complete modeling is performed on the apparent 250-km reflector, including comparisons of its amplitude to that of likely structures as well as possible contamination from *2s1p* arrivals.

Another feature of interest in our migrated images is an apparent vertical offset of the 250- and 410-km discontinuities at 450–500 km *x* offset. This is roughly coincident with the "hinge line" or "hinge zone," the boundary between thin cratonal sedimentary deposits to the east and thick miogeoclinal deposits of westernmost North America, which is thought to mark the circa 700 Ma rift shoulder of cratonic North America [e.g., *Stewart*, 1970; *Levy and Christie-Blick*, 1989; *Moores*, 1991]. Lithosphere to the east of the hinge line (right side of plot) represents the orginal North American Precambrian lithosphere, and lithosphere to the west of the hingeline (left side of plot) was assembled after the rifting event. The offset in the 250- and 410-km discontinuities at this boundary may reflect preserved variations in mantle properties between the Laurentia supercontinent and younger accreted continental material. The 660-km discontinuity shows no corresponding vertical offset at this distance, suggesting that the differences in Precambrian and Paleozoic lithosphere are restricted to shallower depth.

One uncertainty in our analysis is the possible biasing effects of three-dimensional discontinuity structure that is off-axis from our receiver array. In some cases, these structures could falsely project features into our two-dimensional model. To fully resolve this issue will require deployment of a two-dimensional receiver array rather than our one-dimensional line array and full three-dimensional migration of the data. The proposed USArray experiment of thousands of broadband receivers across the United States [*Levander et al.*, 1999] would provide a wealth of data for analyses of this type.

6. Conclusions

The experiments presented here demonstrate the feasibility and utility of migration-style processing of receiver functions for crust and mantle discontinuity imaging. This processing is particularly useful for resolving nonplanar or laterally discontinuous features. Application of these techniques to data from the Snake River Plain PASSCAL experiment show a strong 660-km discontinuity, a weak 410-km discontinuity, and several bright spots at 250 km depth. The 660-km discontinuity shows a region of elevated discontinuity topography roughly coincident with the regions of low upper mantle velocity imaged beneath the SRP and is consistent with the presence of a deep mantle source for the Yellowstone hotspot. The 410-km discontinuity is complex in this region, but the exact details of its structure are not well-imaged. The migration processing presented here is fairly simple, and future developments might include a fuller use of amplitude information, the use of a conjugate gradient style inversion rather than backprojection, and/or an extension of these techniques to invert for three-dimensional structures from a two-dimensional surface array of receivers such as that planned in the USArray experiment. Our tests also show the importance of random resampling tests in assessing the robustness of subtle features.

References

Agee, C. B., and D. Walker, Static compression and olivine flotation in ultrabasic silicate liquid, *J. Geophys. Res.*, *93*, 3437-3449, 1988.

Anderson, D. L., The deep structure of continents, *J. Geophys. Res.*, *84*, 7555-7560, 1979.

Anderson, D. L., *Theory of the Earth*, Blackwell Sci., Malden, Mass., 1989.

Anderson, D. L., and C. Sammis, Partial melting in the upper mantle, *Phys. Earth Planet. Inter.*, *3*, 41-50, 1970.

Archambeau, C. B., E. A. Flinn, and D. G. Lambert, Fine structure of the upper mantle, *J. Geophys. Res.*, *74*, 5825-5865, 1969.

Beucler, E., S. Chevrot, and J. P. Montagner, The Snake River Plain experiment revisted. Relationships between a Farallon plate fragment and the transition zone, *Geophys. Res. Lett.*, *26*, 2673-2676, 1999.

Bina, C. R., and G. Helffrich, Phase transition Clapeyron slopes and transition zone seismic discontinuity topography, *J. Geophys. Res.*, *99*, 15,853-15,860, 1994.

Bostock, M.G., *Ps* conversions from the upper mantle transition zone beneath the Canadian landmass, *J. Geophys. Res.*, *101*, 8393-8402, 1996.

Bostock, M. G., and S. Rondenay, Migration of scattered teleseismic body waves, *Geophys. J. Int.*, *137*, 732-746, 1999.

Castle, J. C., and K. C. Creager, Seismic evidence against a mantle chemical discontinuity near 660 km depth beneath Izu-Bonin, *Geophys. Res. Lett.*, *24*, 241-244, 1997.

Claerbout, J. F., *Earth Soundings Anaysis: Processing Versus Inversion*, Blackwell Sci., Malden, Mass., 1992.

Collier, J. D., and G. Helffrich, Topography of the "410" and "660" km seismic discontinuities in the Izu-Bonin subduction zone, *Geophys. Res. Lett.*, *24*, 1535-1538, 1997.

Dueker, K. G., and E. Humphreys, Relationships between upper mantle velocity structure and the tectonic parabola along the Yellowstone volcanic trend, *Eos Trans. AGU*, *74*(43), Fall Meet. Suppl., F602, 1993.

Dueker, K. G., and A. F. Sheehan, Mantle discontinuity structure from mid-point stacks of converted *P* to *S* waves across the Yellowstone hotspot track, *J. Geophys. Res.*, *102*, 8313-8327, 1997.

Dueker, K. G., and A. F. Sheehan, Mantle discontinuity structure beneath the Colorado Rocky Mountains and High Plains, *J. Geophys. Res.*, *103*, 7153-7169, 1998.

Efron, B., and R. Tibshirani, Statistical data analysis in the computer age, *Science*, *253*, 390-395, 1991.

Flanagan, M. P., and P. M. Shearer, Global stacking of topography on transition zone velocity discontinuities by stacking *SS* precursors, *J. Geophys. Res.*, *103*, 2673-2692, 1998a.

Flanagan, M. P., and P. M. Shearer, Topography on the 410-km seismic velocity discontinuity near subduction zones from stacking of *sS*, *sP*, and *pP* precursors, *J. Geophys. Res.*, *103*, 21,165-21,182, 1998b.

Flanagan, M.P., and P.M. Shearer, A map of topography on the 410-km discontinuity from PP precursors, *Geophys. Res. Lett.*, *26*, 549-552, 1999.

Gaetani, G.A., P.D. Asimow, and E.M. Stolper, Determination of the partial molar volume of SiO2 in silicate liquids at elevated pressures and temperatures: A new experimental approach, *Geochim. Cosmochim. Acta*, *62*, 2499-2508, 1998.

Gaherty, J. B., and T. J. Jordan, Lehmann discontinuity as the base of an anisotropic mechanical boundary layer beneath continents, *Science*, *268*, 1468-1471, 1995.

Gilbert, H. J., A. F. Sheehan, D. A. Wiens, S. Webb, and L. M. Dorman, Receiver function imaging of upper mantle discontinuity structure below the Lau Basin spreading center and Tonga subduction zone, *Eos Trans. AGU*, *79*(45), Fall Meet. Suppl., F641, 1998.

Grand, S. P., and D. Helmberger, Upper mantle shear structure of North America, *Geophys. J. Int.*, *76*, 399-438, 1984.

Gu, Y., A. M. Dziewonski, and C. B. Agee, Global de-correlation of the topography of transition zone discontinuities, *Earth Planet. Sci. Lett.*, *157*, 57-67, 1998.

Gurrola, H., T. J. Owens, A. A. Nyblade, and C. A. Langston, Imaging the mantle transition zone beneath East Africa using telseismic *Ps* converted phases, *Eos Trans. AGU*, *79*(45), Fall Meet. Suppl., F580-581, 1998.

Harjes, H. P., et al., Origin and nature of crustal reflections: Results from integrated seismic measurements at the KTB superdeep drilling site, *J. Geophys. Res.*, *102*, 18,267-18,288, 1997.

Kampfmann, W., A study of diffraction-like events on DEKORP2-S by Kirchhoff theory, *J. Geophys.*, *62*, 163-174, 1988.

Kennett, B.L.N. (Ed.), *IASPEI 1991 Seismological Tables*, Res. Sch. of Earth Sci., Aust. Natl. Univ., Canberra, 1991.

Kosarev, G., R. Kind, S. V. Sobolev, X. Yuan, W. Hanka, and S. Oreshin, Seismic evidence for a detached Indian lithospheric mantle beneath Tibet, *Science*, *283*, 1306-1309, 1999.

Lehmann, I., Velocities of longitudinal waves in the upper part of the Earth's mantle, *Ann. Geophys.*, *15*, 93-118, 1959.

Lehmann, I., *S* and the structure of the upper mantle, *Geophys. J. R. Astron. Soc.*, *4*, 124-138, 1961.

Levander, A., E. D. Humphreys, G. Ekstrom, A. A. Meltzer, and P. M. Shearer, Proposed project would give unprecedented look under North America, *Eos Trans. AGU*, *80*, 245, 250-251, 1999.

Levy, M., and N. Christie-Blick, Pre-Mesozoic palinspastic reconstruction of the eastern Great Basin, *Science*, *245*, 1454-1462, 1989.

Li, A., K. M. Fischer, M. E. Wysession, and T. J. Clarke, Mantle discontinuities and temperature under the North American continental keel, *Nature*, *395*, 160-163, 1998a.

Li, A., K. M. Fischer, M. Wysession, and T. J. Clarke, Upper mantle and transition zone discontinuities beneath eastern North America, *Eos Trans. AGU*, *79*(17), Spring Meet. Suppl., S215, 1998b.

Miller, G. H., E. M. Stolper, and T.J. Ahrens, The equation of state of a molten komatiite, 2, Application to komatiite petrogenesis and the Hadean mantle, *J. Geophys. Res.*, *99*, 11,831-11,848, 1991.

Moores, E. M., Southwest U.S.-East Antarctic (SWEAT) connection: A hypothesis, *Geology*, *19*, 425-428, 1991.

Revenaugh, J., A scattered-wave image of subduction beneath the Transverse Ranges, *Science*, *268*, 1888-1892, 1995.

Revenaugh, J. S., and S. A. Sipkin, Seismic evidence for silicate melt atop the 410-km mantle discontinuity, *Science*, *369*, 474-476, 1994a.

Revenaugh, J. S., and S. A. Sipkin, Mantle discontinuity structure beneath China, *J. Geophys. Res.*, *99*, 21,911-21,927, 1994b.

Revenaugh, J. S., and T. H. Jordan, Mantle layering from *ScS* reverberations; 3, The upper mantle, *J. Geophys. Res.*, *96*, 19,781-19,810, 1991.

Rigden, S., T. J. Ahrens, and E. M. Stolper, Densities of liquid silicates at high pressures, *Science*, *226*, 1071-1074, 1984.

Ryberg, T., M. Weber, and R. Kind, Receiver function arrays: A seismic approach, *Eos Trans. AGU*, *79*(45), Fall Meet. Suppl., F646, 1998.

Saltzer, R., and E. D. Humphreys, Upper mantle *P* wave velocity structure of the eastern Snake River Plain and its relationship to geodynamic models of the region, *J. Geophys. Res.*, *102*, 11,829-11,841, 1997.

Schutt, D., E. D. Humphreys, and K. Dueker, Anisotropy of the Yellowstone hot spot wake, eastern Snake River Plain, Idaho, *Pure Appl. Geophys.*, *151*, 443-462, 1998.

Shearer, P. M., Global mappping of upper mantle reflectors from long-period *SS* precursors, *Geophys. J. Int.*, *115*, 878-904, 1993.

Shearer, P. M., M. P. Flanagan, and M. A. H. Hedlin, Experiments in migration processing of *SS* precursor data to image upper mantle discontinuity structure, *J. Geophys. Res.*, *104*, 7229-7242, 1999.

Sheehan, A. F., P. M. Shearer, H. Gilbert, and K. G. Dueker, Seismic migration processing of *P-SV* converted phases for mantle discontinuity imaging, paper presented at 11th Annual Incorporated Research Institutions for Seismology Workshop, Yosemite, Calif., June 1999.

Shen, Y., A. Sheehan, K. Dueker, C. de Groot-Hedlin, and H. Gilbert, Mantle discontinuity structure beneath the southern East Pacific Rise (MELT experiment region) from *P-to-S* converted phases, *Science*, *280*, 1232-1235, 1998a.

Shen, Y., S. C. Solomon, I. T. Bjarnason, and C. J. Wolfe, Seismic evidence for a lower-mantle origin of the Iceland Plume, *Nature*, *395*, 62-65, 1998b.

Solomatov, S., and D. J. Stevenson, Can sharp seismic discontinuities be caused by non-equilibrium phase transformations?, *Earth Planet. Sci. Lett.*, *125*, 267-279, 1994.

Stewart, J. H., Upper Precambrian and Lower Cambrian strata in the southern Great Basin, U.S. Geol. Surv Prof. Pap., *620*, 206 pp., 1970.

Stolper, E., D. Walker, B. H. Hager, and J. F. Hays, Melt segregation from partially molten source regions: The importance of melt density and source region size, *J. Geophys. Res.*, *86*, 6261-6271, 1981.

Van der Lee, S., and G. Nolet, Seismic image of the trailing edge of the Farallon plate, *Nature*, *386*, 266-269, 1997.

Van der Lee, S., H. Paulssen, and G. Nolet, Variability of *P660s* phases

as a consequence of topography of the 660 km discontinuity, *Phys. Earth Planet. Inter.*, *86*, 147-164, 1994.

Vidale, J. E., and H. M. Benz, Upper mantle seismic discontinuities and the thermal structure of subduction zones, *Nature*, *356*, 678-683, 1992.

Vinnik, L., S. Chevrot, and J. P. Montagner, Evidence for a stagnant plume in the transition zone?, *Geophys. Res. Lett.*, *24*, 1007–1010, 1997.

Wicks, C. W., and M. A. Richards, A detailed map of the 660-kilometer discontinuity beneath the Izu-Bonin subduction zone, *Science*, *261*, 1424-1427, 1993.

Wood, B. J., The effect of H_2O on the 410-kilometer seismic discontinuity, *Science*, *268*, 74-76, 1995.

A. F. Sheehan, H. J. Gilbert, and K. G. Dueker, Department of Geological Sciences, University of Colorado, Boulder, CO 80309. (afs@terra.colorado.edu; hersh@lithos.colorado.edu; ken@lithos.colorado.edu)

P. M. Shearer, Scripps Institution of Oceanography, 9500 Gilman Drive, La Jolla, CA 92093-0225. (shearer@mahi.ucsd.edu)